Electron Microscopy Structure Study of Laser-Clad TiC-Ni Particle-Reinforced Coating

J.H. Ouyang, Xiaodong Li, and T.C. Lei

(Submitted 18 August 1999; in revised form 19 September 1999)

The microstructure of a laser-clad TiC-Ni particle-reinforced coating on 1045 steel was studied by scanning electron microscopy (SEM), transmission electron microscopy (TEM), and ion microprobe mass spectroscopy (IMMS). The microstructural constituents of the clad layers (CLs) were analyzed to be TiC particles, γ-Ni primary dendrites, and interdendritic eutectics of γ_E-Ni plus $M_{23}(CB)_6$ and $M_6(CB)$ carboborides. Three growth mechanisms of the original TiC particles were found: (1) stepped lateral growth at the edges, (2) radiated and cylindrically coupled growth at the edges, and (3) bridging growth of the clustered particles. Ordered and modulated structures were found in the original TiC particles. In addition to the original TiC particles, fine TiC particles precipitated from the liquid phase and γ-Ni solid solution during laser cladding. The microstructures of the bonding zones (BZs) were intimately associated with laser processing parameters. The BZs of the clad coatings can be categorized into three types according to the combination of the CL with heat-affected zone (HAZ): (1) straight interface combination, (2) zigzag connection, and (3) combination by partial melting of prior austenitic grain boundaries of the substrate. The straight interface BZ consists of the γ-Ni solid solution only, but in the other two types of combinations, the BZs consist of γ-Ni primary dendrites, γ-(Fe, Ni)/$M_{23}(C, B)_6$ eutectics, and martensite of the substrate. The microstructural evolution of the CLs was discussed. The formation and phase transformation models of the BZs were proposed.

Keywords laser cladding, TiC-Ni particle, 1045 steel, microstructure

1. Introduction

Laser cladding of metal-ceramic composite coatings has shown high potential in manufacturing wear-resistant coatings for ambient and high-temperature performance. Previous studies[1-5] showed that reinforcing particles (WC, TiC, SiC, and CrB_2) were partially dissoluted during laser cladding. Precipitates, such as intermetallics, carbides, and borides, nucleated and grew during solidification. In the laser-clad coating reinforced with TiC and WC particles, the extent of partial dissolution of the WC particles was much higher than that of the TiC particles because WC particles have higher thermal diffusivity and lower volume free energy than TiC particles.[1] The morphology difference of the original TiC particles and the TiC precipitates was found in laser-clad TiC-reinforced coatings on a Ti-6Al-4V alloy, an iron-base alloy, and a 5052Al alloy.[2] In a laser-clad CrB_2-reinforced coating on steel 1045, microstructural constituents of the clad coating were found to be Cr_3C_2, Fe_3B, and $(Fe, Cr)_xB_y$, as well as the original CrB_2 particles.[3] Although much research has been completed on the characterization of these precipitates,[1-5] very little is understood about their nucleation and growth mechanisms.

Laser cladding processes develop metallurgical bonding by intermixing or interdiffusing of elements across the interface. Due to the big difference in composition between clad coating and steel substrate, considerable transport of elements occurs at the interface, which greatly affects its bonding strength and its resistance against wear or corrosion. The metallurgical continuity of the substrate, coupled with fusion bonding between the clad coating and substrate, means that spalling or delamination can be avoided.

Several theoretical models of the microstructural formation in laser surface alloying have been suggested.[6] Based on the local growth conditions, the concept of microstructural selection was introduced. A good metallurgical bond between laser-clad NiCrAl coating and 316L stainless steel substrate was found.[7] However, the addition of zirconia particles to the NiCrAl coating induced intergranular cracks, although the incorporation of the particles was designed to reinforce the coating. Therefore, the conventional coating design concept cannot be used in laser cladding. To widely use the laser cladding technique, studies on laser cladding structure and phase transformations are needed.

2. Experimental Procedure

Commercial steel 1045 with a chemical composition (wt.%) of 0.43C-0.22Si-0.52Mn-0.01P-0.02S was used as the substrate. A mixture of 30 vol.% TiC particles and 70vol.% nickel-alloy powders was used as a coating material. The chemical composition (wt.%) of the nickel-alloy powders with an average size of 40 μm was 15.0Cr-4.0B-5.8Si-0.73C-12.3Fe, and its geometry was spherical. The TiC particles less than 4 μm in size had an irregular shape. The thickness of the preplaced mixture was 0.5 min. A 2 kW continuous wave CO_2 laser was employed to produce the coating under the following conditions of 700 to 1000 W laser power, 2 to 4 mm beam diameter, and 1 to 14 mm/s traverse speed. An argon atmosphere was used to shroud the molten pool from the surrounding air.

In order to examine the microstructures of bonding zones (BZs), heat-affected zones (HAZs) of the steel, and clad layers (CLs), specimens large enough to include all these regions were sliced from the clad coating. Specimens for scanning electron microscopy (SEM) studies were prepared by conventional mounting,

J.H. Ouyang, Fraunhofer Institute for Material and Beam Technology, D-01277 Dresden, Germany; **Xiaodong Li,** and **T.C. Lei,** School of Materials Science and Engineering, Harbin Institute of Technology, Harbin 150001, People's Republic of China. Contact e-mail: li.233@osu.edu.

grinding, and polishing methods. The specimens were first etched with 3% nital solution to reveal the microstructure of the HAZs. Subsequently, electrolytic etching was carried out to reveal the microstructure of the CLs using a 10 *M* NaOH solution. Foils for transmission electron microscopy (TEM) examination were prepared using the ion beam thinning technique. Microstructural observations were carried out using a Hitachi S570 (Hitachi Ltd., Tokyo) scanning electron microscope and a Philips CM12 (Philips Electronics North America, New York, NY) transmission electron microscope.

3. Results

3.1 Microstructural Characteristics of the Laser-Clad TiC Particle-Reinforced Coating

Figure 1 shows the microstructure of the laser-clad TiC-Ni particle-reinforced coating. The coating consists of TiC particles, γ-Ni primary dendrites (γ_P), and interdendritic eutectics of γ-Ni (γ_E), plus $M_{23}(C, B)_6$ and $M_6(C, B)$ carboborides. Energy dispersive x-ray (EDX) microanalysis showed that the stoichiometric

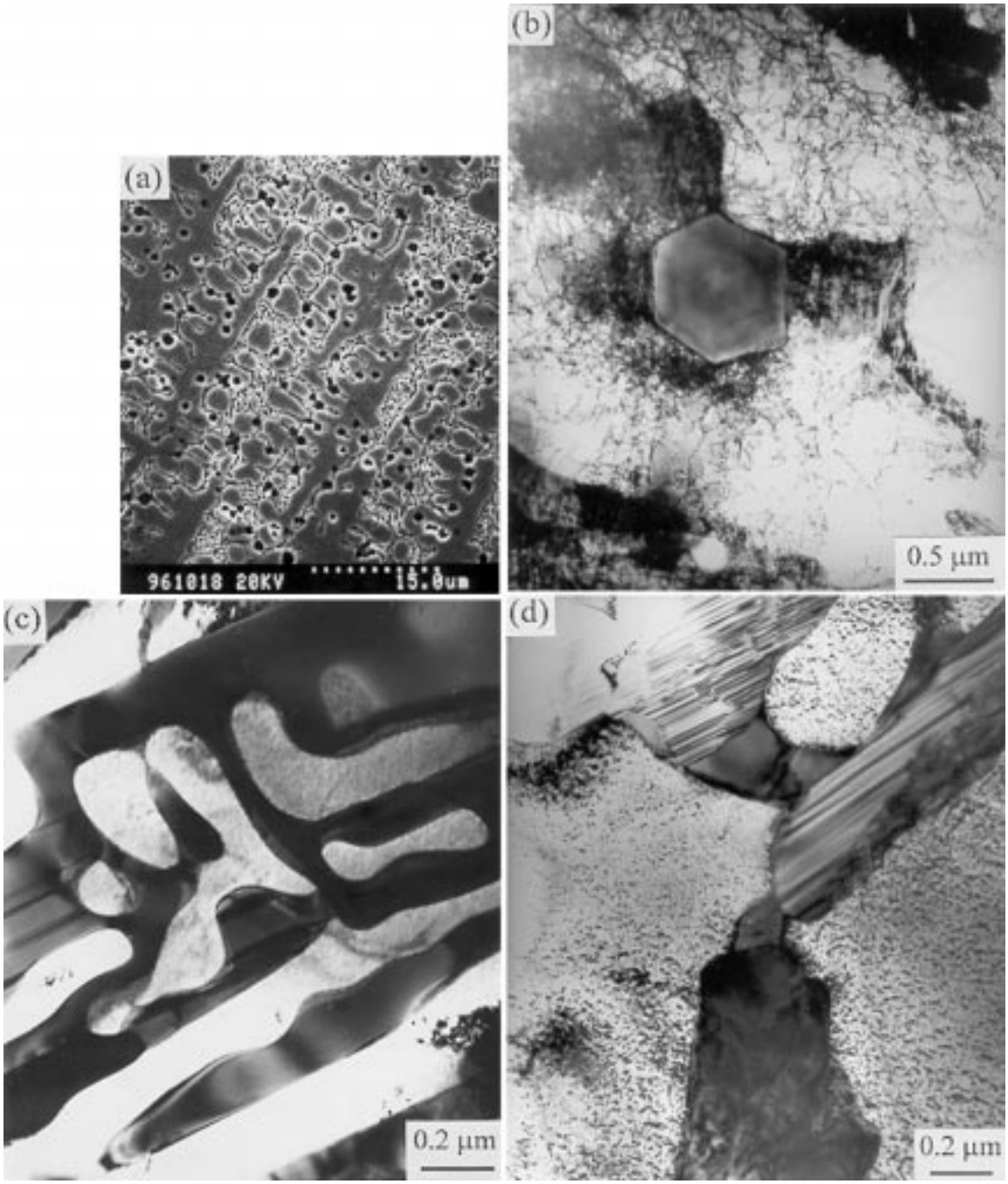

Fig. 1 Microstructure of the laser-clad TiC-Ni particle-reinforced coating. **(a)** CL. **(b)** TiC particle. **(c)** interdendritic eutectics. **(d)** eutectic carboborides, $M_{23}(C, B)_6$ with stacking fault and $M_6(C, B)$ without stacking fault

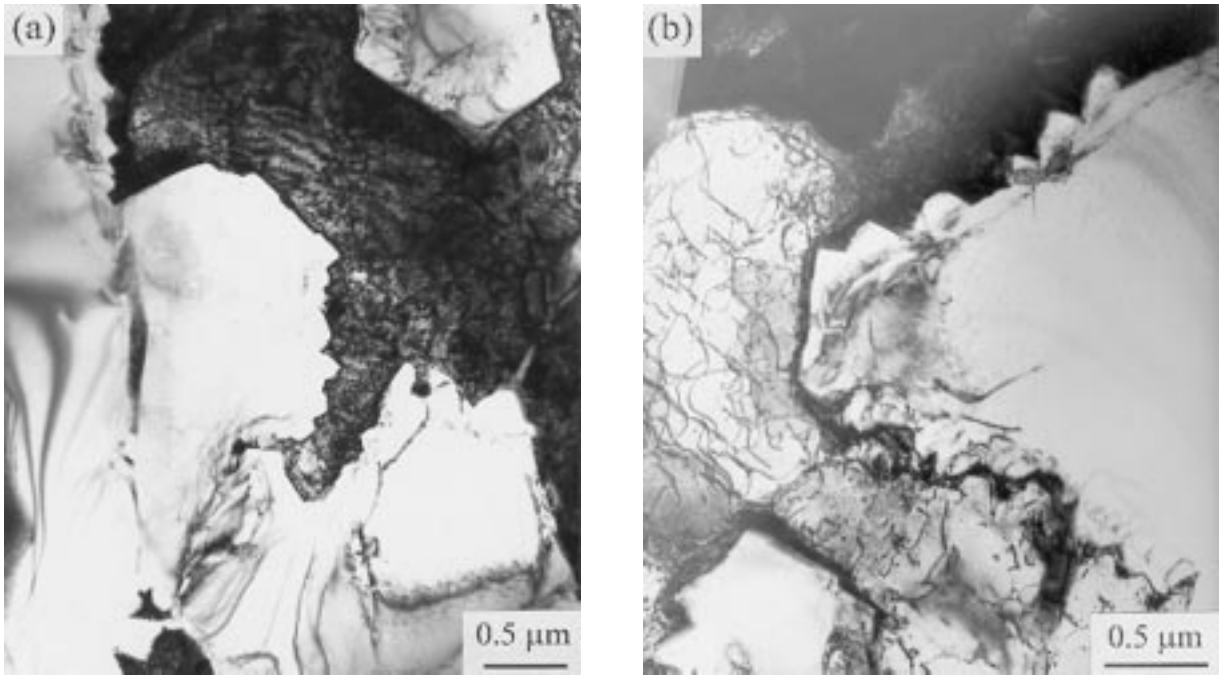

Fig. 2 Morphology of the stepped lateral growth at the edges of the original TiC particles. **(a)** Continuous step growth. **(b)** Discontinuous step growth

formula of the $M_{23}(C, B)_6$ phase was $(Cr_{0.583}, Fe_{0.396}, Ni_{0.016}, Si_{0.002}, Ti_{0.003})_{23}(C, B)_6$ and the stoichiometric formula of the $M_6(C, B)$ phase was $(Cr_{0.228}, Fe_{0.686}, Ni_{0.057}, Si_{0.024}, Ti_{0.005})_6(C, B)$. Transmission electron micrographs show heavily dislocated substructures in the primary dendrites and the eutectic matrix (Fig. 1b to d). Stacking fault fringes were found in the $M_{23}(C, B)_6$ carboborides, but not in the $M_6(C, B)$ carboborides (Fig. 1d). It is well known that the cooling rates are inversely proportional to the spacing of the dendrite arms.[8] Based on the spacings between primary dendrites, as shown in Fig. 1(a), the cooling rates were calculated to be in the range of 3.23×10^3 to 1.15×10^4 °C/s. At such a high cooling rate, laser cladding not only refines the primary dendrites and interdendritic eutectics, but also produces γ-Ni solid solution with a supersaturation of titanium, chromium, carbon, and boron and a high density of dislocations. The ED microanalysis indicated that a large amount of titanium atoms exist in the primary dendrites and eutectic matrix due to partial dissolution of the original TiC particles. During cooling, titanium and carbon atoms in the laser molten pool may tend to precipitate at certain cooling speeds because of the decrease of solid solubility.

Growth of the Original TiC Particles. Figure 2 shows the morphology of the stepped lateral growth at the edges of the original TiC particles. Continuous (Fig. 2a) and discontinuous (Fig. 2b) step-growth structures with different orientations are observed at the edges of the original TiC particles. This suggests that a basic octahedron crystal unit composed of one titanium atom and six carbon atoms piles up along the TiC <111> directions. Changes in local temperature or concentration gradient on the TiC {111} planes led to the formation of sawtooth morphology at the edges of the particles.

Figure 3 shows the morphology of the radiated and cylindrically coupled growth at the edges of the original TiC particles. A fine eutectic-like structure composed of TiC_E and γ_E-Ni solid solution is observed at the edges of the original TiC particles. Figure 3(c) and (d) show the schematic of the formation mechanisms of the TiC_E/γ_E-Ni eutectics. Selected area electron diffraction (SAD) analysis indicates that the lattice constant of the TiC_E is about $a_o = 0.45$ nm, which is slightly higher than that of the original TiC particles (0.433 nm). This was mainly attributed to the existence of chromium and iron atoms in the TiC_E, which was confirmed by EDX microanalysis at the positions A, B, and C in Fig. 3(a). It was found that the TiC_E was obtained only at a faster cooling speed (above 10^5 °C/s) in coordination with the diffusion of alloy elements except titanium toward the lateral matrix, which is very analogous to the eutectics reaction labeled $L \rightarrow TiC_E + \gamma$ at the edges of the original TiC particles, where L indicates the liquid phase. In this eutectic reaction, TiC_E is the leading phase of the nucleation.

Figure 4 shows a typical bridging growth of the clustered TiC particles. The TiC crystal nucleates at the edges of the original particles and then grows toward the center of clusters. The SAD analysis at the center of clusters indicates that the lattice constant of TiC was approximately $a_o = 0.437$ nm. No other elements except titanium were revealed by EDX (with carbon and boron excluded) at the measurement position A. The bridging connection of the clustered TiC particles resulted in a dramatic increase in TiC particle size.

Ordered Structure in the Original TiC Particles. The ordered structure was observed in the original TiC particles, as shown in Fig. 5. In Fig. 5(a), the bright area is the normal structure of TiC crystal with a faceted feature, and the three dark areas are the ordered structure of the TiC crystal. No other elements except titanium were found by EDX (with carbon and boron excluded). Figure 5(c) and (d) give the SAD patterns of

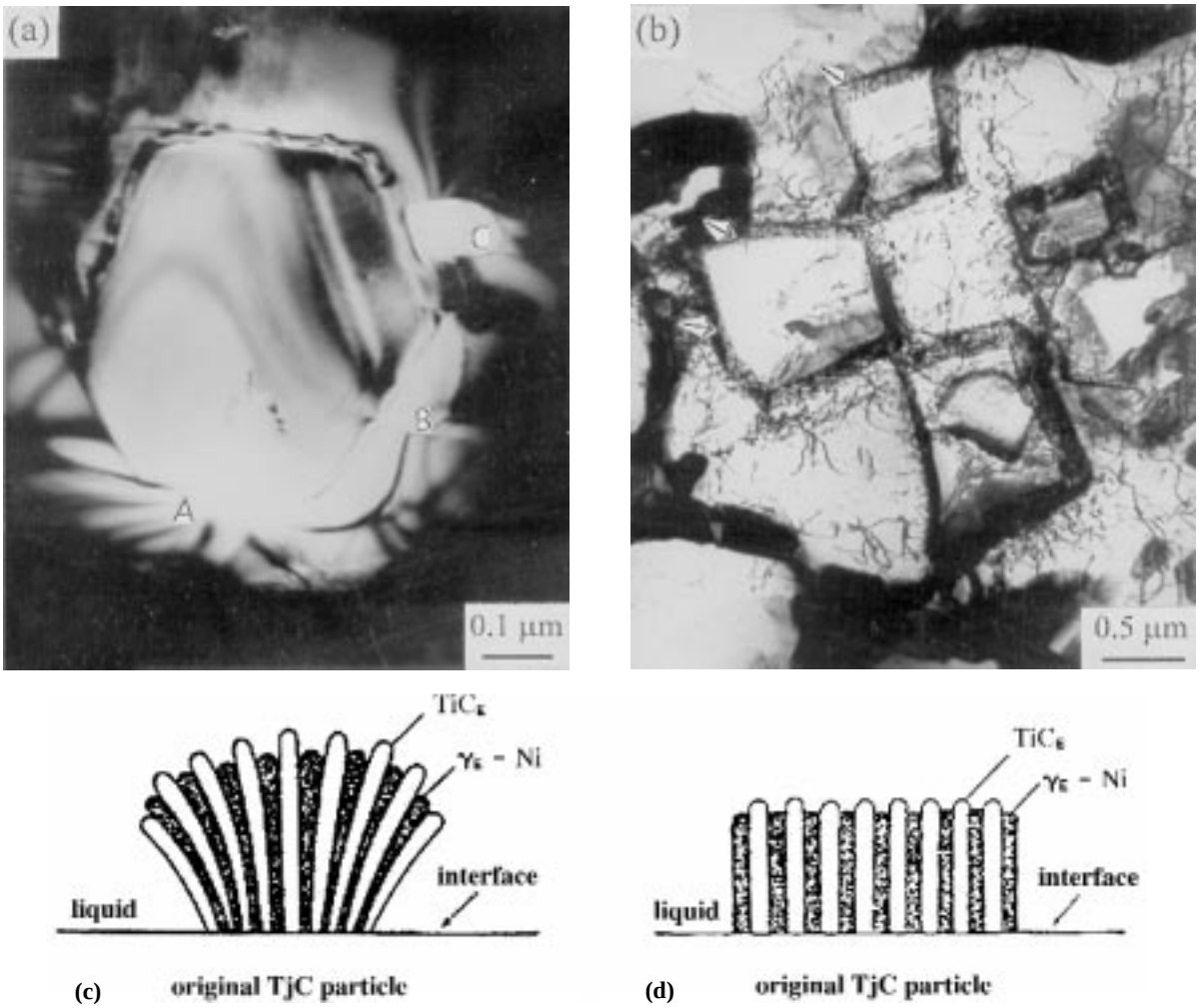

Fig. 3 Morphology of the radiated and cylindrically coupled growth at the edges of the original TiC particles. **(a)** and **(c)** Radiated coupled growth. **(b)** and **(d)** Cylindrically coupled growth

the normal structure and the ordered structure, respectively. The SAD patterns of the ordered structure contain two sets of extra forbidden spots labeled by (-1/3, -5/3, 1/3) type and (-2/3, -10/3, 2/3) type spots with a zone axis of [015]. The dark-field image (Fig. 5b) taken by using the {-1/3, -5/3, 1/3} type forbidden spot clearly shows the ordered structure of the TiC particles. A modulated structure was observed in the TiC particles, which was believed to result from the ordered arrangement of carbon vacancies in the TiC particles. The TiC crystal generally exhibited a wide face-centered cubic (fcc) phase field accompanied by the changes of carbon concentration at the octahedron interstitial positions. In general, some of the octahedron interstitial positions of crystal lattice were occupied by carbon atoms and the others remained vacant. During partial dissolution of the original TiC particles at high temperature, carbon atoms diffused from the interior of the particles to the matrix and resulted in the carbon vacancy diffusion toward the interior of particles. If the increase of carbon vacancies in the TiC particles caused an ordered rearrangement of vacancies, a modulated structure was formed within the TiC particles or at their edges.

Precipitation of TiC from Liquid Phase. Figure 6 shows the TEM micrographs of the branchlike TiC precipitates. The TiC precipitates have a typical faceted structure with distinct arris features (Fig. 6a) and are believed to independently nucleate and grow from liquid phase. The outer side plane of arris structure was analyzed to be the TiC {111} planes with the lowest growth speed. The SAD analysis (Fig. 6b) indicates that the orientation relationship between the TiC precipitates and γ-Ni solid solution is $[112]_{TiC} \parallel [112]_{\gamma\text{-Ni}}$ and $(111)_{TiC} \parallel (111)_{\gamma\text{-Ni}}$.

Precipitation of TiC from γ-Ni Solid Solution. Below the solidification temperature of TiC, fine TiC particles precipitated independently from the γ-Ni solid solution because of the decrease of the solid solubility of titanium and chromium atoms in the γ-Ni primary dendrites. These TiC precipitates exhibit cubic-shaped morphology with a size of approximately 0.04 to 0.13 μm, as shown in Fig. 7. The EDX data revealed no other elements except titanium in the precipitates (with carbon and boron excluded). The SAD analysis indicates that the lattice constant of the TiC precipitates was α_o = 0.438 nm. Note that these TiC precipitates nucleate at the lattice defects with high energy, such as dislocations (Fig. 7). The nucleation and growth of

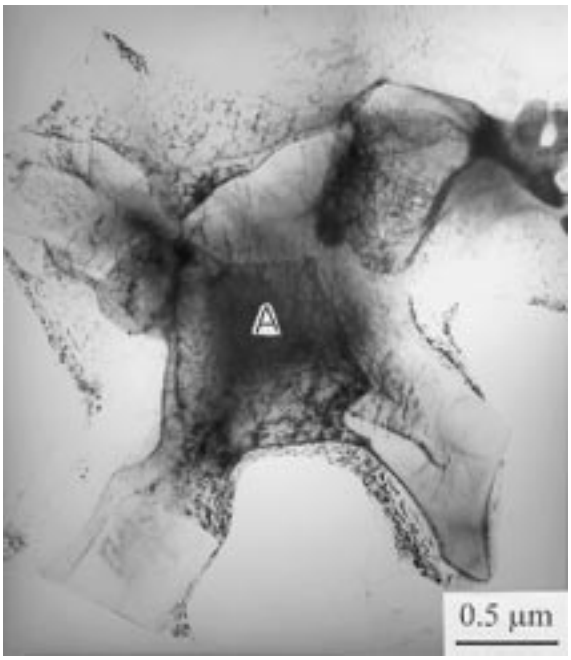

Fig. 4 Transmission electron micrograph showing a typical bridging growth of the clustered TiC particles

the TiC precipitates mainly depended on the diffusion of titanium and carbon atoms.

3.2 Microstructural Characteristics of the BZs

The microstructure of the BZ was considerably complicated and mainly dependent upon laser processing parameters. To clearly describe the variations in microstructural features of BZ, three types of BZs were differentiated from each other according to the combination mode between the CL and the HAZ of the substrate.

Straight Interface Combination. Straight interface combination was obtained at laser power density less than 80 W/mm^2 and high traverse speed. Figure 8 shows the microstructure of the BZ. The BZ was found to be a single fcc γ-Ni solid solution with a lattice constant of a_o = 0.37 nm. The width of the BZ was in the range of 2.5 to 14 μm. Heavily dislocated substructures are observed in the BZ (Fig. 8b), which are believed to result from rapid solidification.

Table 1 shows the compositions (weight percent) of different regions in and around the BZ obtained by ion microprobe mass spectroscopy (IMMS). Alloy elements were intermixed in the BZ, and iron was diluted in the CL. A sharp drop of the concentration of the elements, particularly chromium and nickel, was found at the interface, indicating the absence of extensive interdiffusion. It was interesting to note that some of the iron in the substrate was diffused into the CL. In the area of the CL close to the coating/substrate interface, a thin band of planar growth was observed, which was believed to be due to the highest temperature gradient and lowest solidification rate at the initial stages of solidification.[9] As solidification proceeded, planar growth stopped due to interfacial instabilities and dendritic solidification occurred within a short distance from the interface.

Zigzag Connection. At laser power density of 72 W/mm^2, as traverse speed was decreased from 8 to 4 mm/s, a transition of the BZ from a straight interface to a zigzag interface occurred. This was the result of heterogeneous melting at the boundaries of the HAZ caused by a long time interaction between laser beam and clad material. The BZ was partitioned into two regions featured by fully molten and partially molten zones, as shown in Fig. 9. In order to clearly analyze the variations in microstructural features, the microstructures with different features are marked by letters I, II, and III, as indicated in Fig. 9(a). Region I was determined to be γ-Ni solid solution with planar interface; region II consisted of primary dendrites and interdendritic eutectics; and region III consisted of primary dendrites, interdendritic eutectics, and martensite (α') of the substrate. Localized melting traces can be observed in the partially molten zone. When the traverse speed was decreased to 2 mm/s, a typical zigzag morphology was observed, as shown in Fig. 9(b) and (c). It can be seen that the solidification begins in either columnar or dendritic form epitaxially from the grain boundaries of HAZ. The TEM observations revealed that all the planar and primary dendritic crystals in the BZs were γ-Ni austenitic phase with high density of dislocations. The interdendritic eutectics consisted of γ_E-Ni and $M_{23}(C, B)_6$ carboborides.

The authors found that laser energy was preferably conducted along the grain boundaries, as marked by arrows in Fig. 9(d). This was because grain boundaries have high energy and rapid diffuse paths, which lead to localized melting at the grain boundaries during laser cladding. During solidification, γ-Ni primary dendrites and interdendritic eutectics were formed at the localized molten region of the grain boundaries.

Microvoids were observed in the front of the solidified grain boundaries. Contraction caused by solidification was considered to be associated with the formation of microvoids. Figure 10 shows the distribution of carbon and boron elements near the molten grain boundaries in the partially molten region obtained by IMMS. It can be found that the molten grain boundaries in the partially molten region were rich in carbon (0.9 wt.%) and boron (0.6 wt.%), but only 0.25 wt.% carbon was detected in the grain interior. Carboboride was observed to precipitate in the partially molten region after solidification because of the high carbon and boron concentrations in that area.

Partial Melting of the Prior Austenitic Grain Boundaries of Substrate. The morphology of the BZ formed under the condition of 120 W/mm^2 power density and 4 mm/s traverse speed is shown in Fig. 11, which exhibits a typical phenomenon of preferable melting at prior austenitic grain boundaries. The BZ can be partitioned into two regions, BZ1 and BZ2. A planar interface was found between these two regions and shares the same grain. The grain boundaries in the BZ1 and BZ2 regions consisted of the eutectics of γ_E-Ni and $M_{23}(C, B)_6$ because of higher laser power density, as contrasted to the molten grain boundaries including γ-Ni primary dendrites and eutectics in the zigzag connection BZ. Many fine precipitates and small microvoids can be observed in the molten grain boundaries, as shown by the arrows in Fig. 11(b).

Figure 12 shows the TEM micrographs of the BZ1 and BZ2 regions. The BZ1 region consists of γ-Ni primary dendrites with dense dislocations and the eutectics of γ_E-Ni and $M_{23}(C, B)_6$ carboborides. The stoichiometric formula of the $M_{23}(C, B)_6$

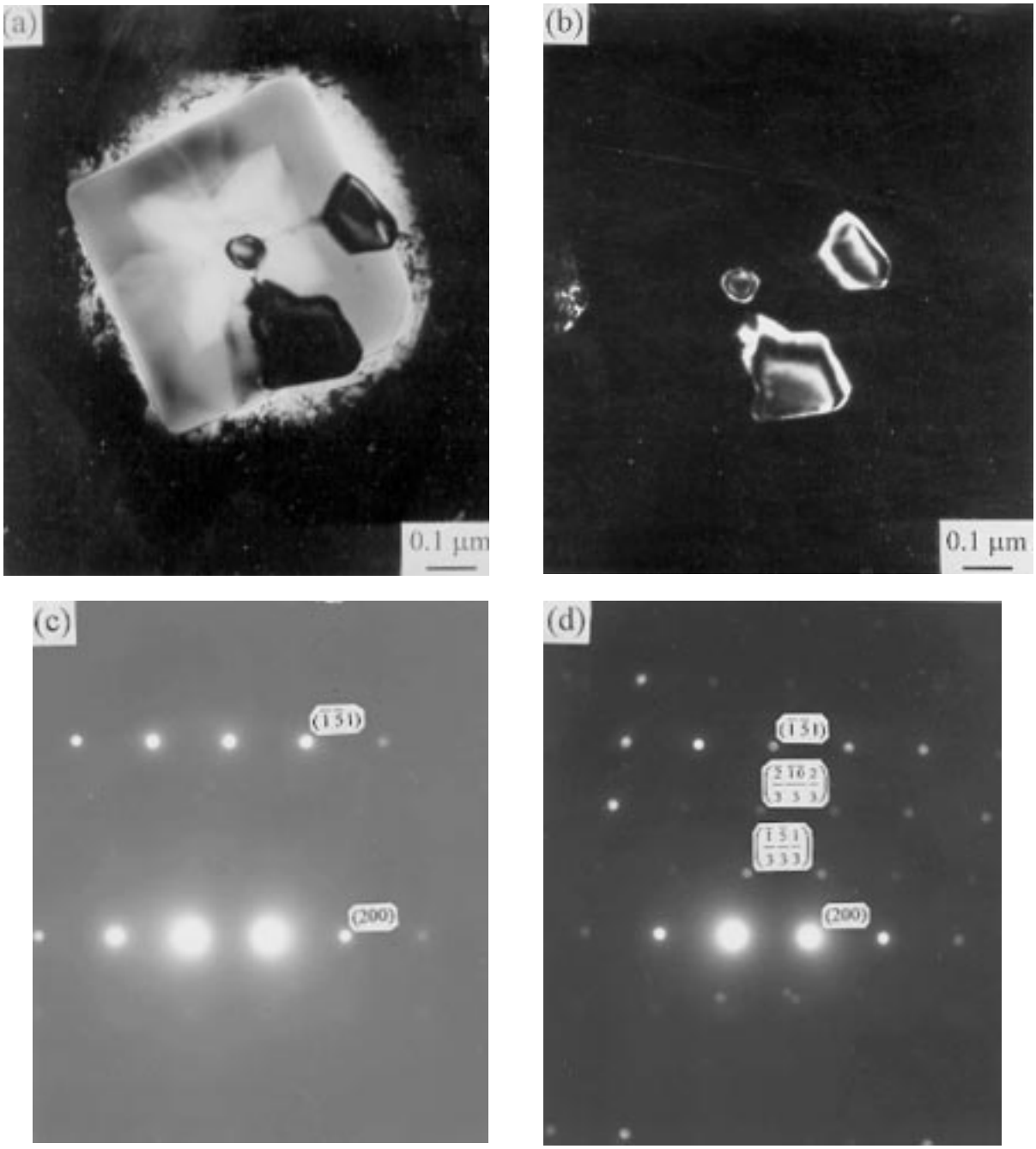

Fig. 5 Ordered structure in the original TiC particles. **(a)** Bright-field TEM image. **(b)** Dark-field TEM image taken by using a (1/3, 5/3, 1/3) type forbidden spot in **(d). (c)** and **(d)** SAD patterns of the normal structure and ordered structure, respectively

Table 1 Compositions of different regions near the interface between the clad layer and HAZ revealed by ion microprobe mass spectroscopy

	Composition, wt.%						
Measurement position	**Ni**	**Cr**	**Fe**	**Si**	**Ti**	**C**	**B**
Primary dendrite	64.36	9.35	16.54	3.81	3.72	0.83	1.39
Eutectic	36.25	24.23	25.78	4.89	2.41	1.56	4.88
Bonding zone	53.26	10.22	27.42	3.31	1.3	0.65	3.84
HAZ	0	0	99.58	0	0	0.42	0

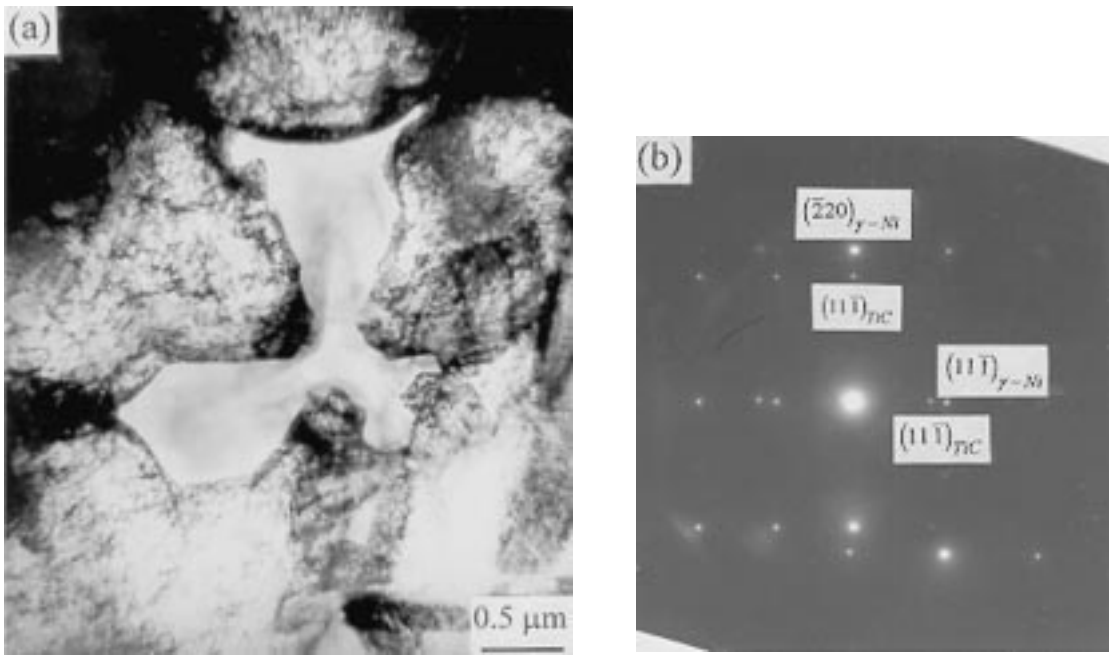

Fig. 6 The TiC particle precipitated from the liquid phase. **(a)** Bright-field TEM image. **(b)** SAD pattern from the $[112]_\gamma$ direction showing the orientation relationship between γ-Ni and TiC

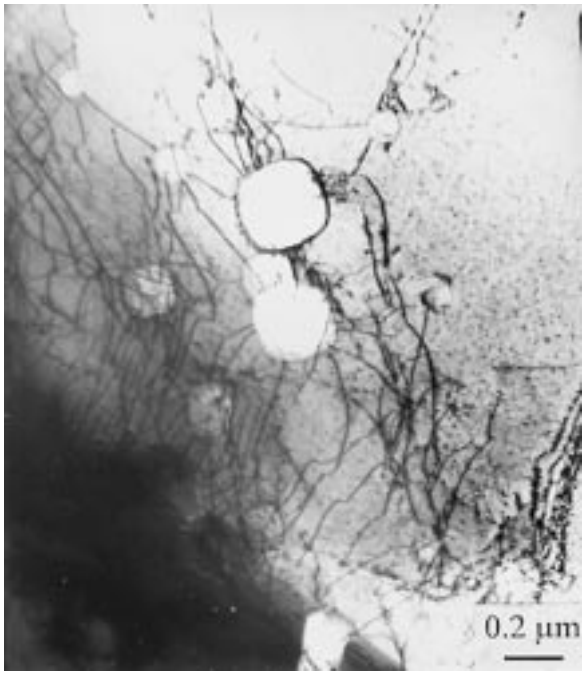

Fig. 7 The TiC particles precipitated from γ-Ni solid solution

carboborides was determined to be $(Fe_{0.5}Ni_{0.1}Cr_{0.4})_{23}(C, B)_6$ by EDX, and the lattice constant of the carboborides was about 1.067 nm.

The eutectic carboborides in the BZ2 region exhibited a net structure around the eutectic matrix with a high density of dislocations, as shown in Fig. 12(b). Table 2 shows the compositions (weight percent) of various phases obtained by EDX. The eutectic was severely saturated by alloy elements as a result of intermixing of chromium, nickel, and iron atoms. Large quantities of alloy elements were found to diffuse into the molten grain boundary regions.

In the BZ2 region, inside the grains with partially molten grain boundaries, lath-type martensite with a width of 0.2 μm was found (Fig. 13a). The martensite contained a high density of dislocations (Fig. 13b). Figure 14 shows the distribution of carbon and boron elements across the prior austenitic grains with partially molten boundaries obtained by IMMS. The molten grain boundaries were rich in carbon (0.7 wt.%) and boron (0.12 wt.%). Only 0.3 wt.%C was detected inside the grains. The boron atoms detected in the molten grain boundaries were considered to come from coating materials. The high carbon contents in grain boundaries were attributed to the anomalous uphill diffusion from grain interior to grain boundaries.

4. Discussion

The following discussion will focus first on the microstructural evolution of the clad coatings and then on the concentration profile and models of formation and phase transformations of BZs under various laser cladding conditions.

4.1 Microstructural Evolution of the Clad Coatings

Laser cladding of a TiC-Ni particle-reinforced coating not only refines the primary dendrites and the interdendritic eutectics, but also produces γ-Ni solid solution with supersaturation of titanium, chromium, carbon, and boron elements. In such a high solidification process, a high concentration of lattice defects such as the stacking faults in the eutectic carboborides, the dislocations in the dendrites and the eutectic matrix, and the carbon vacancies with an ordered rearrangement in TiC particles is pro-

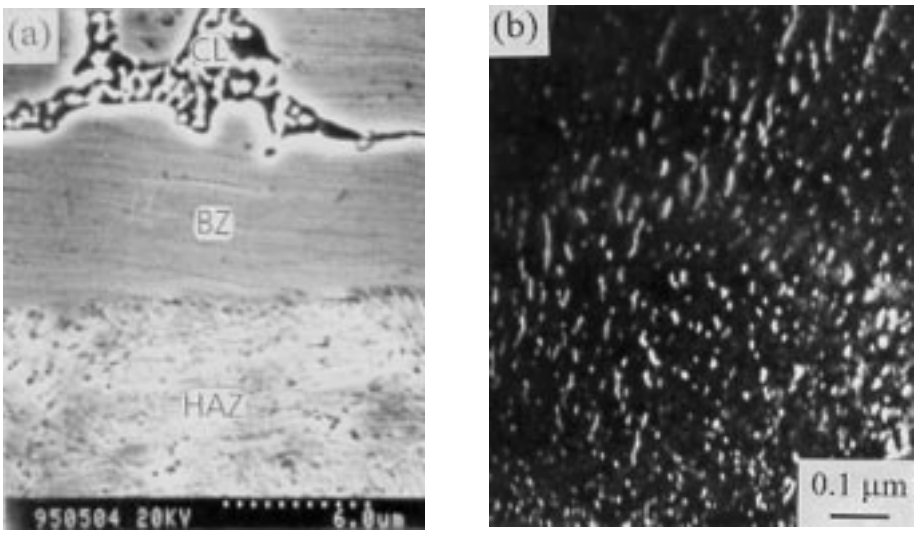

Fig. 8 Microstructural features in and around the bonding zone. **(a)** Straight interface combination (SEM). **(b)** γ-Ni with high density of dislocations in bonding zone (TEM)

Table 2 Compositions of various phases indicated in Fig. 12(b) revealed by EDX analysis on TEM foils (with carbon and boron, excluded)

	Composition, wt. %				
Measurement position	**Ni**	**Cr**	**Fe**	**Si**	**Ti**
Eutectic matrix	21.77	3.25	73.24	0.98	0.76
Eutectic carboboride	0.74	38.43	60.83	0	0

duced in the clad coating rapidly cooled from the molten state. Depending on the velocity at the liquid/solid interface, different spacings and eutectic morphologies can be formed. The average interdendritic spacing was between 1.5 and 3 μm, and the possible cooling rates were estimated to be 10^3 to 10^5 °C/s. An average interlamellar spacing of the eutectic morphologies was about 50 μm. The fine grain strengthening of the alloy matrix together with the TiC hard phase strengthening greatly enhanced the microhardness and wear resistance of clad coating.[5]

For such a complex TiC-Ni-Cr-B-Si-Fe-C alloy system used in this study, it is difficult to find the equilibrium phase diagram, and no data can be used to analyze the nonequilibrium solidification process presented. According to the previously mentioned results, the possible sequence of phase transformations in the primary dendrites (γ_P-Ni) and the eutectic matrix (γ_E-Ni) during solidification of laser-clad TiC-Ni particle-reinforced coating can be represented as follows:

$$70\text{vol.\%Ni alloy} + 30\text{vol.\%TiC} \rightarrow L + \text{TiC}_\text{I} \rightarrow L + \text{TiC}_\text{I} + \text{TiC}_\text{II} \rightarrow \gamma_P + L_E + \text{TiC}_\text{I} + \text{TiC}_\text{II} \rightarrow (\gamma_P + \text{TiC}_\text{III}) + \{\gamma_E + \text{M}_{23}(\text{C, B})_6 + \text{M}_6(\text{C, B})\} + \text{TiC}_\text{I} + \text{TiC}_\text{II}$$

where L indicates the liquid phase produced by laser irradiation, and the subscripts I, II, and III represent undissolved TiC particles, TiC precipitates from liquid phase, and γ_P-Ni solid solution, respectively.

4.2 Concentration Profiles of the Bonding Zones

As indicated previously, the formation process of BZs can be visualized to be the process of fusion bonding between the clad coating and the substrate. The elements from the melted region of steel are incorporated and homogenized with the coating material in the liquid phase, which provides a greater degree of intermixing and minimizes the gradient across the bonding zones. Because the diffusion of nickel to the molten region of base steel stabilizes the austenite of BZs, γ-(Fe, Ni) solid solution will remain stable at room temperature instead of martensite.

Although some titanium atoms can be detected in the BZs, no original TiC particles can be found there. As an independent reinforcement, the TiC particles tend to move toward the upper region of the CL as a result of their lower density compared with nickel alloy and the boost by the intense convection of the molten pool. Even if a small number of TiC particles stay in the liquid near the pool/substrate interface, they will be pushed away by the solid/liquid interface advancing at the lowest speed during the initial stage of solidification.[5] This is very different from the explanation given by Singh and Mazumder,[10] who suggested that the evolved latent heat energy during solidification could lead to the melting of an additional layer of the substrate and that there was not enough time for it to remix with the remelting melt, so that the lower section of BZs would be rich in substrate and contain no undissolved hafnium particles in laser-clad Ni-Cr-Al-Hf coating.

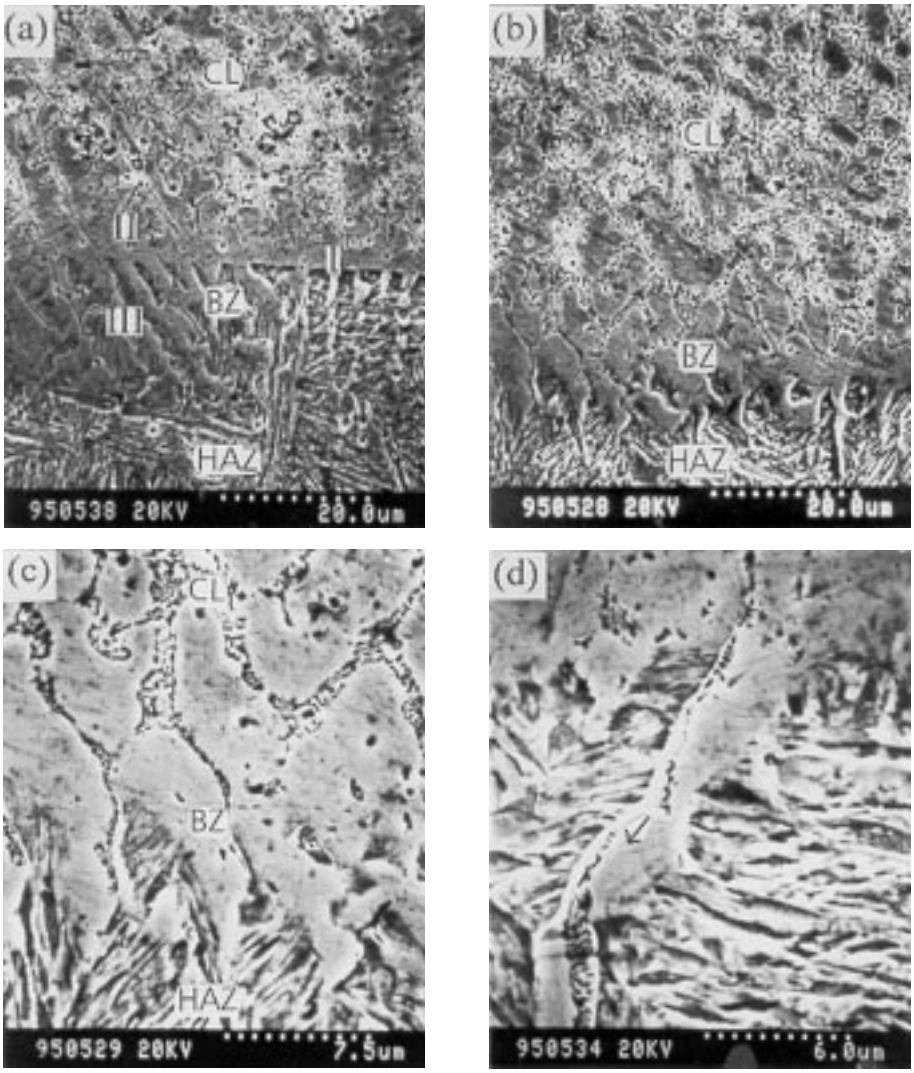

Fig. 9 Microstructural features of the bonding zone with a zigzag connection (BZ1—fully molten zone, and BZ2—partially molten zone). **(a)** Transition from straight interface combination to zigzag connection. **(b)** and **(c)** Zigzag connection. **(d)** Localized melting at the grain boundaries

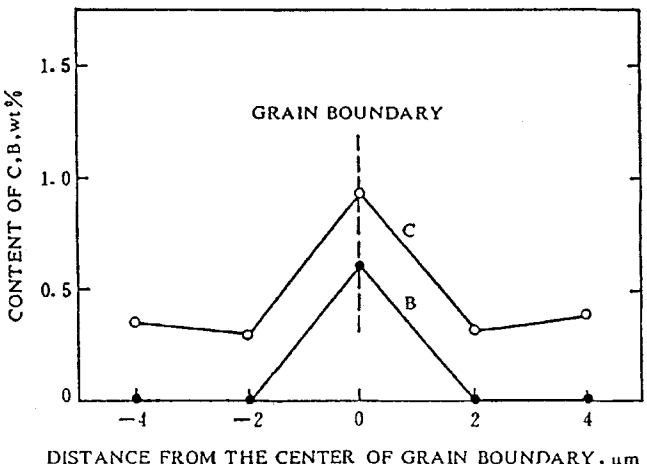

Fig. 10 Distribution of carbon and boron elements near the molten grain boundaries in the partially molten region

A distinct characteristic in the BZ is the heterogeneous distribution of the different elemental species, especially the segregation of carbon and boron at the molten grain boundaries in the BZ. In the BZ2 region, the higher concentration of the carbon at the grain boundary regions than in the grain interior, which is even much lower than that of the 1045 steel, indicated that an anomalous uphill diffuse occurred from the grain interior to grain boundary regions. The carbon diffusion process was controlled by the chemical potential of the whole system, which was associated with the concentration coefficients of carbon in different phases. The following factors could be responsible for the migration of carbon. (a) Low carbon partition coefficients under the condition of the coexistence of solid-liquid phase in the BZ2 region. Because the carbon partition coefficient, k_o, in iron- carbon alloys is only about $k_o = 0.13$, it leads to diffusion of carbon atoms from the grain interior with a high chemical potential grain interior to molten grain boundaries with a low chemical potential and finally causes the segregation of carbon. If the cooling rate is slow enough, the degree of segregation will continue to increase. (b)

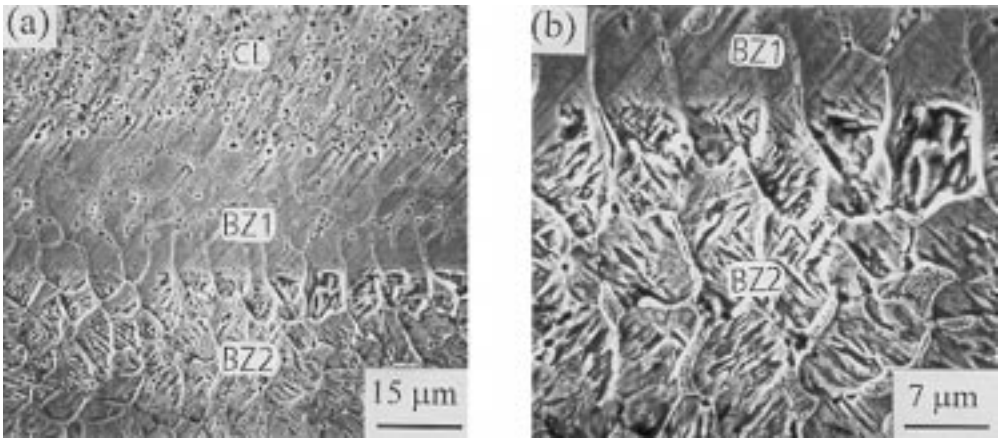

Fig. 11 Typical molten grain boundaries of the boundary zone (BZ1—fully molten zone, and BZ2—partially molten zone). **(a)** Boundary zone. **(b)** Precipitates and microvoids in the molten grain boundaries

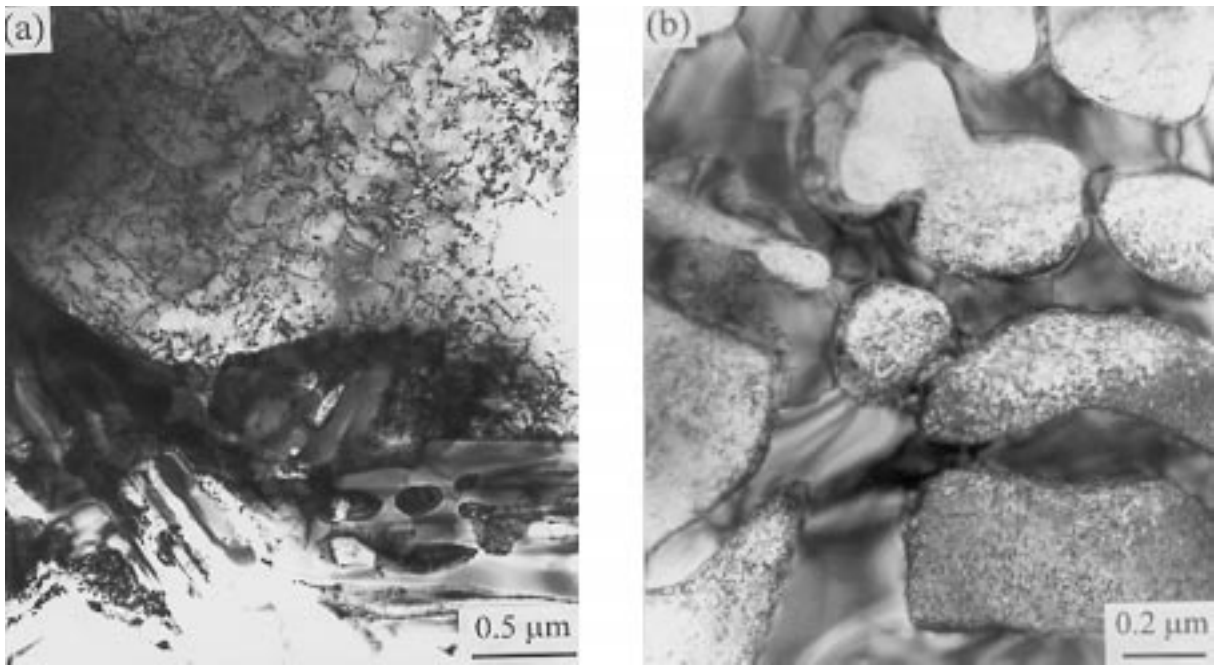

Fig. 12 TEM photographs showing the microstructure of the BZ1 and BZ2 regions. **(a)** γ-Ni primary dendrites and interdendritic eutectics in the BZ1 region. **(b)** Eutectics in the BZ2 region

Enhanced kinetics of carbide precipitation reaction in the presence of nickel. (c) Decreased carbon concentration coefficient, which was caused by the precipitation of carboborides and diffusion of chromium and titanium atoms into the molten grain boundaries.

4.3 Formation and Phase Transformation Models of the Bonding Zones

As previously mentioned, the microstructure of BZs mainly depends upon the laser processing parameters. The outline of the molten pool interface is not simply a straight interface and sometimes exhibits an irregular zigzag interface, or even a more severely tilted curve.

This heterogeneously melting phenomenon of the substrate is summarized as being caused by the following reasons. (a) The high energy structures of HAZs such as the grain boundaries, phase boundaries, or other structural defects can be preferably melted by laser energy. (b) The flowing of liquid and movement of the TiC particles at the bottom of the laser molten pool probably exert influence on the thermal conducting toward the substrate from the coating.

Based on the observations and discussion described previously, models were proposed to explain the formation and phase transformation of the BZs in the clad coating. Figures 15 to 17 give the schematic models of the formation and phase transformations of the BZs.

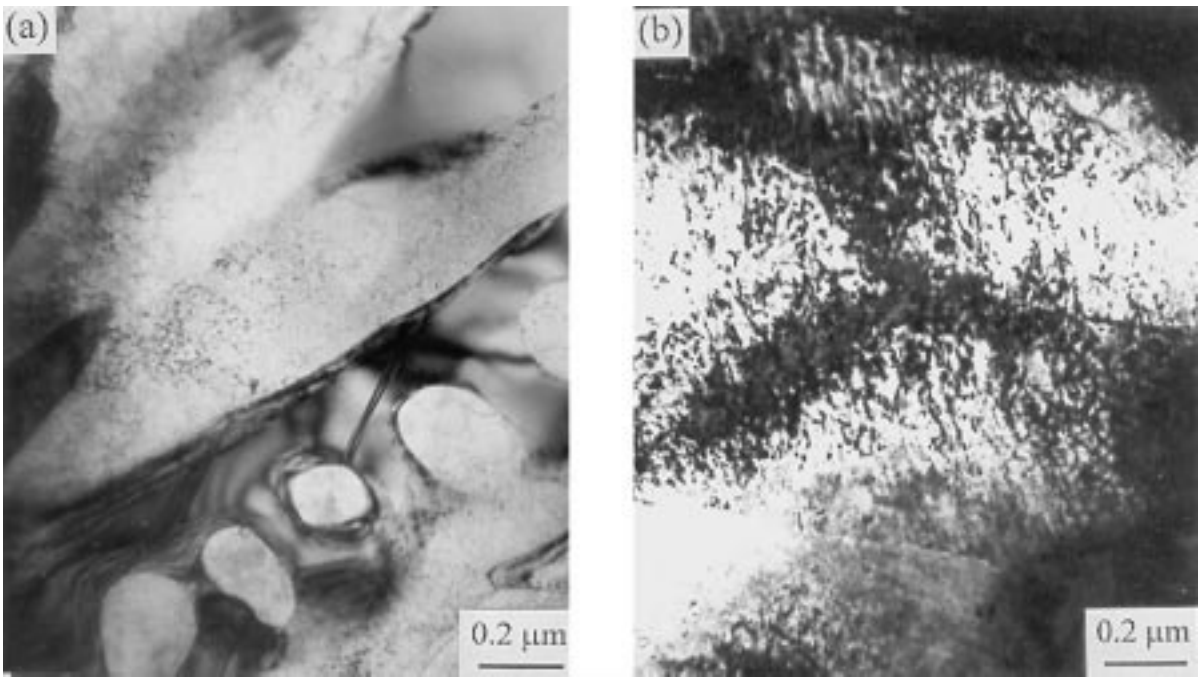

Fig. 13 Microstructure of the molten grain boundary area (BZ2) near the melting interface. **(a)** Bright-field image showing martensite near the melting interface. **(b)** High density of dislocations in the martensite

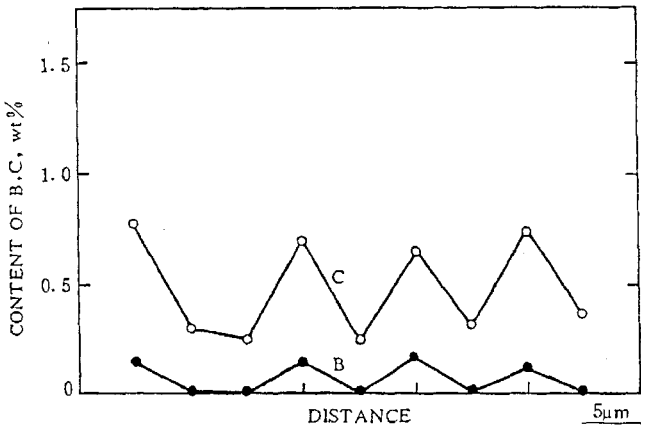

Fig. 14 Distribution of carbon and boron elements in the BZ2

Figure 15 shows the schematic of the formation and phase transformation of the BZ with a straight interface. At faster traverse speed of laser beam, only a very thin layer of the substrate rapidly melts in a short time with an even molten pool/substrate interface, and the concentration of alloy elements in the melt near the interface is lower with respect to that formed at slower traverse speed because of insufficient time for mixing and diffusing of the liquids. Because the ratio of the thermal gradient, *G*, to the solidification speed, *R*, near the interface is very high, a planar growth is possible at the initial stages of solidification. However, the very rapid increase of *R* during solidification often destabilizes this planar growth before a stationary state is reached after cooling to room temperature, and a thin band of planar growth was obtained in the bonding zones and was analyzed to be single γ-Ni solid solution. As solidification proceeded, planar growth stopped due to interfacial instabilities, and a dendritic/eutectic structure occurred within a short distance from the interface.

Figure 16 shows the schematic of the formation and phase transformation characteristics of the BZ with a zigzag connection to the substrate. At slower traverse speed, higher solute concentration and lower thermal gradient were beneficial to the cellular-dendritic growth just at the beginning, based on the constitutional undercooling theory.[11] Under the condition of the higher laser power density and slower traverse speed, the liquid phase has time enough to reject the excess solute into the interdendritic areas where the eutectic finally forms. Moreover, the substrate melts more deeply and spreads from the molten grain boundaries before solidification so that the molten pool/substrate interface is uneven and exhibits a heterogeneous melting of the substrate. Two regions (BZ1 and BZ2) were partitioned because of the heterogeneous melting of the substrate. After cooling to room temperature, the BZ1 consisted of γ_P and the eutectics of γ_E and $M_{23}(C, B)_6$, and the BZ2 contained γ_P and the eutectics in the solidified grain boundaries, while lath martensite remained in the grain interior.

Figure 17 shows the formation and phase transformation characteristics of the BZ with a combination by partial melting of prior austenitic grain boundaries. As contrasted to the phase constituents indicated in Fig. 16, the distinct difference in phase constituents was that no γ-Ni primary dendrites existed in the molten grain boundaries of the BZ2. The two similar regions (BZ1 and BZ2) can be divided from the BZ.

5. Conclusions

The following conclusions can be drawn.

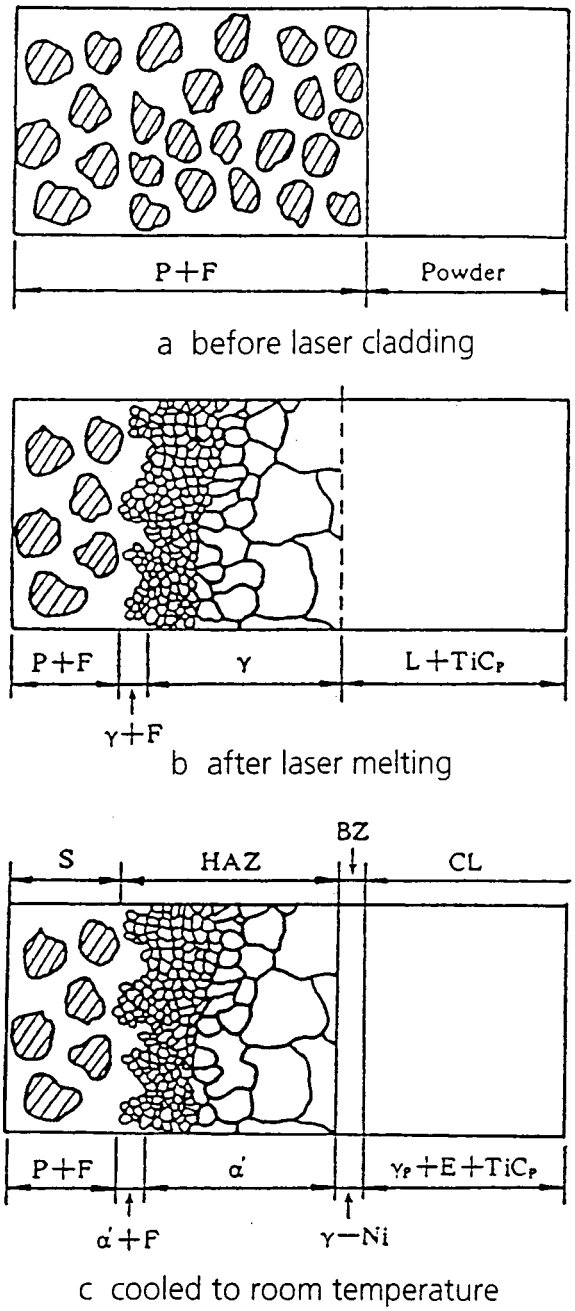

Fig. 15 **(a)** to **(c)** Schematic model snowing the formation and phase transformation of the boundary zone with a straight interface (P = pearlite, F = ferrite, γ = austenite, L = liquid, α' = fine martensite, TiC_P = TiC particle, E = eutectics of γ_E-Ni plus $M_{23}(C, B)_6$, and γ_P = primary γ-Ni dendrite)

- The microstructural constituents of the CL were analyzed to be TiC particles, γ-Ni primary dendrites, and interdendritic eutectics of γ_E-Ni plus $M_{23}(C, B)_6$ and $M_6(C, B)$ carboborides.
- Three growth mechanisms of original TiC particles were found: stepped lateral growth at the edges, radiated, and cylindrically coupled growth at the edges and bridging growth of the clustered particles.

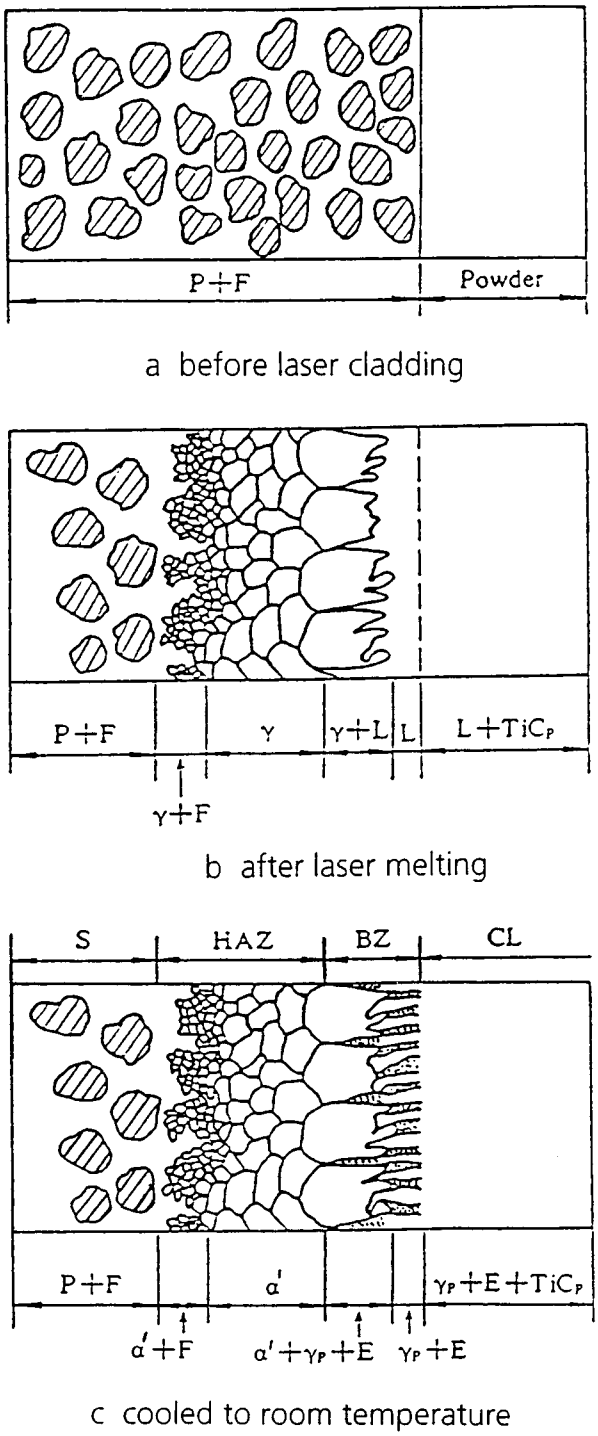

Fig. 16 **(a)** to **(c)** Schematic model showing the formation and phase transformation of the bonding zone with a zigzag connection (P = pearlite, F = ferrite, γ = austenite, L = liquid, α' = fine martensite, TiC_P = TiC particle, E = eutectics of γ_E-Ni plus $M_{23}(C, B)_6$, and γ_P = primary γ-Ni dendrite)

- Ordered and modulated structures were observed in the original TiC particles and were considered to be caused by the ordered rearrangement of carbon vacancies in the TiC particles.
- In addition to the original TiC particles, fine TiC particles

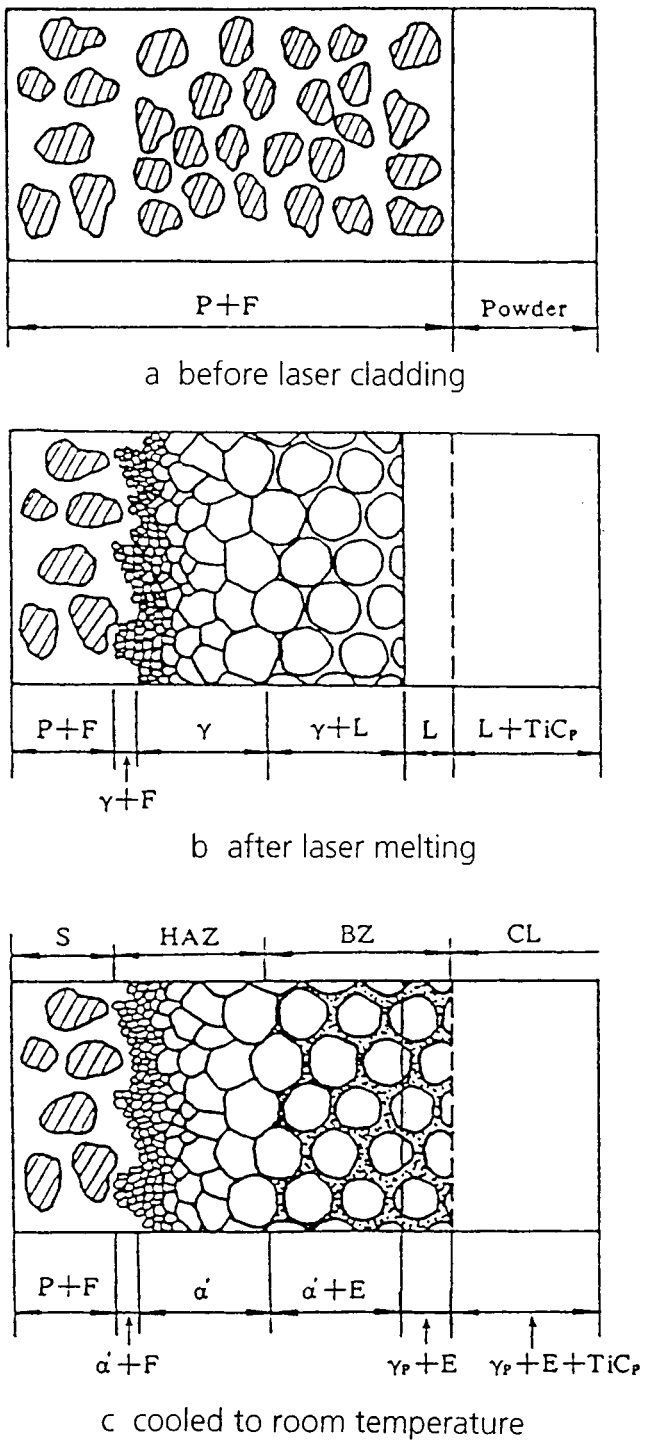

Fig. 17 **(a)** to **(c)** Schematic model showing the formation and phase transformation of the boundary zone with a combination by partial melting of prior austenitic grain boundaries (*P* = pearlite, *F* = ferrite, γ = austenite, *L* = liquid, α' = fine martensite, TiC_P = TiC particle, *E* = eutectics of γ_E-Ni plus $M_{23}(C, B)_6$, and γ_P = primary γ-Ni dendrite)

precipitated from the liquid phase and γ-Ni solid solution during laser cladding.

- The BZs of the clad coatings can be categorized into three types according to the combination of the CL with HAZ: (a) straight interface combination, (b) zigzag connection, and (c) combination by partial melting of prior austenitic grain boundaries of the substrate. The straight interface BZ consists of the γ-Ni solid solution only, but in the other two types of combinations, the BZs consist of γ-Ni primary dendrites, γ-(Fe, Ni)/$M_{23}(C, B)_6$ eutectics, and martensite of the substrate.

Acknowledgement

One of the authors, Dr. J.H. Ouyang, gratefully acknowledges the financial support from the Alexander von Humboldt Foundation and the Chinese Aerospace Foundation.

References

1. K.P. Cooper: *J. Vac. Sci. Technol. A*, 1986, vol. 4, pp. 2857.
2. J.D. Ayers, R.J. Schaefer, and W.P. Robey: *J. Met.*, 1981, No. 8, pp. 19.
3. G. Shafirstein, M. Bamberger, M. Langohr, and F. Maisenhalder: *Surf. Coat. Technol.*, 1991, vol. 45, pp. 417.
4. J.H. Abboud and D.R.F. West: *J. Mater. Sci. Lett.*, 1991, vol. 10, pp. 1149.
5. T.C. Lei, J.H. Ouyang, Y.T. Pei, and Y. Zhou: *Mater. Sci. Technol.*, 1995, vol. 11, pp. 520.
6. A. Frenk and W. Kurz: *Lasers Eng.*, 1992, vol. 1, pp. 193.
7. J.J. de Damborenea and A.T. Vazquez: *J. Mater. Sci.*, 1993, vol. 28, pp. 4775.
8. M.C. Flemings: *Solidification Processing*, McGraw-Hill, New York, NY, 1974.
9. Y.T. Pei, J.H. Ouyang, and T.C. Lei: *Metall. Mater. Trans. A*, 1996, vol. 27A, pp. 391.
10. J. Singh and J. Mazumder: *Metall. Trans. A*, 1988, vol. 19A, pp. 1981.
11. W. Kurz and D.J. Fisher: *Fundamentals of Solidification*, Trans Tech Publications Ltd., Aedermannsdorf, 1984.